

## Article

# Ni/(R<sub>2</sub>O<sub>3</sub>,CaO) Nanocomposites Produced by the Exsolution of R<sub>1.5</sub>Ca<sub>0.5</sub>NiO<sub>4</sub> Nickelates (R = Nd, Sm, Eu): Rare Earth Effect on the Catalytic Performance in the Dry Reforming and Partial Oxidation of Methane

Sergey A. Malyshev<sup>1,2</sup>, Oleg A. Shlyakhtin<sup>1,\*</sup> , Alexey S. Loktev<sup>3,4,5</sup> , Galina N. Mazo<sup>1</sup> ,  
Grigoriy M. Timofeev<sup>1</sup>, Igor E. Mukhin<sup>4</sup>, Roman D. Svetogorov<sup>6</sup> , Ilya V. Roslyakov<sup>5,7</sup>  
and Alexey G. Dedov<sup>3,4,5</sup>

- <sup>1</sup> Department of Chemistry, M.V. Lomonosov Moscow State University, 119991 Moscow, Russia  
<sup>2</sup> Department of Materials Sciences, Shenzhen MSU-BIT University, Shenzhen 518172, China  
<sup>3</sup> A.V. Topchiev Institute of Petrochemical Synthesis, Russian Academy of Sciences, 119991 Moscow, Russia  
<sup>4</sup> Department of General and Inorganic Chemistry, Gubkin Russian State University of Oil and Gas, 119991 Moscow, Russia  
<sup>5</sup> N.S. Kurnakov Institute of General and Inorganic Chemistry, Russian Academy of Sciences, 119991 Moscow, Russia  
<sup>6</sup> National Research Center “Kurchatov Institute”, 123182 Moscow, Russia  
<sup>7</sup> Department of Materials Sciences, M.V. Lomonosov Moscow State University, 119991 Moscow, Russia  
\* Correspondence: oleg@inorg.chem.msu.ru



**Citation:** Malyshev, S.A.; Shlyakhtin, O.A.; Loktev, A.S.; Mazo, G.N.; Timofeev, G.M.; Mukhin, I.E.; Svetogorov, R.D.; Roslyakov, I.V.; Dedov, A.G. Ni/(R<sub>2</sub>O<sub>3</sub>,CaO) Nanocomposites Produced by the Exsolution of R<sub>1.5</sub>Ca<sub>0.5</sub>NiO<sub>4</sub> Nickelates (R = Nd, Sm, Eu): Rare Earth Effect on the Catalytic Performance in the Dry Reforming and Partial Oxidation of Methane. *Materials* **2022**, *15*, 7265. <https://doi.org/10.3390/ma15207265>

Academic Editors: Theodore E. Matikas and Csaba Balázsi

Received: 29 August 2022

Accepted: 15 October 2022

Published: 18 October 2022

**Publisher's Note:** MDPI stays neutral with regard to jurisdictional claims in published maps and institutional affiliations.



**Copyright:** © 2022 by the authors. Licensee MDPI, Basel, Switzerland. This article is an open access article distributed under the terms and conditions of the Creative Commons Attribution (CC BY) license (<https://creativecommons.org/licenses/by/4.0/>).

**Abstract:** In order to clarify the role of R<sub>2</sub>O<sub>3</sub> in the metal-oxide catalysts derived from complex oxide precursors, a series of R<sub>1.5</sub>Ca<sub>0.5</sub>NiO<sub>4</sub> (R = Nd, Sm, Eu) complex oxides was obtained. A significant systematic increase in the orthorhombic distortion of the R<sub>1.5</sub>Ca<sub>0.5</sub>NiO<sub>4</sub> structure (K<sub>2</sub>NiF<sub>4</sub> type, Cmce) from Nd to Eu correlates with a corresponding decrease in their ionic radii. A reduction of R<sub>1.5</sub>Ca<sub>0.5</sub>NiO<sub>4</sub> in the Ar/H<sub>2</sub> gas mixture at 800 °C causes a formation of dense agglomerates of CaO and R<sub>2</sub>O<sub>3</sub> coated with spherical 25–30 nm particles of Ni metal. The size of metal particles and oxide agglomerates is similar in all Ni/(R<sub>2</sub>O<sub>3</sub>,CaO) composites in the study. Their morphology is rather similar to the products of redox exsolution obtained by the partial reduction of complex oxides. All obtained composites demonstrated a significant catalytic activity in the dry reforming (DRM) and partial oxidation (POM) of methane at 700–800 °C. A systematic decrease in the DRM catalytic activity of composites from Nd to Eu could be attributed to the basicity reduction of R<sub>2</sub>O<sub>3</sub> components of the composite catalysts. The maximum CH<sub>4</sub> conversion in POM reaction was observed for Ni/(Sm<sub>2</sub>O<sub>3</sub>,CaO), while the maximum selectivity was demonstrated by Nd<sub>2</sub>O<sub>3</sub>-based composite. The possible reasons for the observed difference are discussed.

**Keywords:** metal-oxide nanocomposites; multicomponent catalysts; rare earth effect; complex oxide precursors; K<sub>2</sub>NiF<sub>4</sub> structure; exsolution; dry reforming of methane; partial oxidation of methane

## 1. Introduction

Most of the modern catalysts of methane conversion to synthesis gas consist of the nickel nanoparticles allocated at the surface of the various oxide substrates by means of the traditional incipient wetness technique [1–4]. The application of this technique to the synthesis of the modern multicomponent metal-oxide catalysts is rather complicated. In order to solve this problem, several alternative chemical synthesis methods are currently in study. They are based on the reductive decomposition of various precursors containing all the necessary cations of these composites in a single molecule or a chemical compound [5–8]. These techniques ensure the homogeneous spatial distribution and the tight contact of the particles of individual components in the decomposition products.

One of the most promising of these alternative methods is a reduction of complex oxides by hydrogen at elevated temperatures. In the case of the partial reduction of complex oxides, also called a redox exsolution technique, the reduction products consist of the spherical nanoparticles of metal exsolved from the volume of oxide precursor and tightly bound to the surface of micron-sized particles of the partially reduced complex oxides [9–14]. The main advantages of this synthesis technique deal with the enhanced adhesion of metal nanoparticles to the oxide substrate and the possibility of obtaining multicomponent substrates often used in modern catalytic systems. It was recently discovered that similar nanocomposites could be obtained not only from the partial but also from the complete reduction of complex oxides. In this case, reductive decomposition of the complex oxide causes the formation of tightly bound crystallites of the individual oxides covered by the spherical metal nanoparticles [15,16]. Both kinds of reduction products appear to be suitable for application in redox catalysis at elevated temperatures.

The most widely used group of these precursors is complex oxides with a perovskite structure due to their relatively simple synthesis at moderate temperatures and high stability of these compounds at elevated temperatures for exsolution synthesis [17–19]. However, in spite of a wide variety of perovskites, the amount of Ni-containing complex oxides with this structure is rather limited. This constraint deals with the limited stability of the perovskite lattice, usually described as a Goldschmidt's tolerance rule strictly limiting the allowed oxidation states and ionic radii of A cations in the  $\text{ANiO}_3$  lattice. For these reasons, most studies on the perovskite-derived Ni-based catalysts deal with  $\text{LaNiO}_3$  and its solid solutions as precursors. The possibility of obtaining nanocomposites of Ni metal with other oxides from these precursors does not seem reasonable.

These limitations produce serious complications to finding the optimum oxide components of the metal-oxide catalyst. It is known that the oxide substrate or, more generally, the oxide components of the composite Ni/ $\text{MeO}_x$  catalysts have a significant effect on their catalytic performance due to both their own acid–base and redox properties and due to the metal–substrate interactions (MSI) [20,21]. In the case of methane conversion, the application of oxides with an acidic surface in catalysis is not desirable, as it prevents the sorption of  $\text{CO}_2$  in the course of the complex reaction of methane conversion at the surface of catalyst; it also promotes the intense coke formation during its exploitation. For these reasons it is recommended to use metal oxides with significant or strong basicity, like rare earth and/or alkaline earth oxides, in these catalysts [1,22–26]. In order to promote the redox processes at the surface of catalyst, the application of oxides with significant oxygen mobility in their lattice is also helpful. However, the optimum selection of these oxides and their combinations to improve the performance of conversion catalysts is still under consideration.

The application of Ruddlesden–Popper complex oxides as precursors for the Ni/ $\text{MeO}_x$  catalysts opens new ways to study the effect of various rare earth and alkaline earth oxides on the physico-chemical properties and catalytic performance of these composites [27–29]. These  $(\text{R,A})_2\text{NiO}_4$  compounds are known for the several light rare earth elements such as Gd. Due to the stability criteria of  $\text{K}_2\text{NiF}_4$ -like phases, the partial substitution of R with Ca in these nickelates promotes the stabilization of these compounds and allows one to obtain them at lower temperatures [30–35]. The formation of continuous  $\text{R}_{2-x}\text{Ca}_x\text{NiO}_4$  solid solutions allows one to obtain Ni/ $(\text{R}_2\text{O}_3, \text{CaO})$  composites with various R/Ca ratios from single-phase precursors under the same processing conditions, ensuring correct comparison of their physico-chemical and catalytic properties.

It is shown during these studies that the maximum catalytic activity in the POM reaction among Ni/ $(\text{Nd}_2\text{O}_3, \text{CaO})$  composites is demonstrated by the Ca-free Ni/ $\text{Nd}_2\text{O}_3$  counterpart. However, its activity in the DRM reaction is found to be less than that of the others. Meanwhile, the optimum selection of a rare earth element for application in these catalysts with specific morphology remains unclear. For these reasons a synthesis of several  $\text{R}_{2-x}\text{Ca}_x\text{NiO}_4$  precursors (R = Nd, Sm, Eu) is performed in order to compare the

morphology and the catalytic properties of their reduction products in partial oxidation and dry reforming of methane.

## 2. Materials and Methods

### 2.1. Synthesis

In order to obtain  $R_{1.5}Ca_{0.5}NiO_4$  ( $R = Nd, Sm, Eu$ ) by the freeze-drying synthesis method  $Nd_2O_3$ ,  $Sm_2O_3$ ,  $Eu_2O_3$ ,  $CaCO_3$ , and  $Ni(NO_3)_2 \cdot 6H_2O$  were used as precursors.  $Nd_2O_3$ ,  $Sm_2O_3$ , and  $Eu_2O_3$  were annealed at 800 °C for 2 h and  $CaCO_3$  at 400 °C for 1 h before use in order to remove the adsorbed  $H_2O$ . The amount of  $H_2O$  in nickel nitrate was refined by the gravimetric analysis.  $R_2O_3$  and  $CaCO_3$  in the stoichiometric ratios were dissolved in 20% acetic acid; corresponding amount of  $Ni(NO_3)_2 \cdot 6H_2O$  was added. An aqueous solution (5 mass %) of polyvinyl alcohol was added to all solutions under intense stirring. The freeze-drying of flash-frozen solutions was performed in a Labconco FreeZone 7948030 tray dryer (Labconco, Kansas City, MI, USA) at  $P = 0.7$  mbar for 2 days. Thermal decomposition of the freeze-dried products was performed in air at 1200 °C for 6 h. A reduction of as-obtained  $R_{1.5}Ca_{0.5}NiO_4$  powders was performed in an  $H_2:Ar = 1:20$  gas mixture at 850 °C for 1 h followed by slow cooling to room temperature.

### 2.2. Characterization

XRD analysis of the powders was performed using a Rigaku D/MAX-2500PC diffractometer (Rigaku, Tokyo, Japan) with  $Cu K_{\alpha 1}$  radiation generated on a rotating Cu anode (40 kV, 250 mA). More detailed investigation of the  $R_{1.5}Ca_{0.5}NiO_4$  crystal structure was performed using powder diffraction of synchrotron radiation at a wavelength  $\lambda = 0.74$  Å. The measurements were performed using a 2D Rayonix SX165 detector (Rayonix LLC, Evanston, IL, USA) at the XSA (X-ray Structural Analysis) beamline of the Kurchatov synchrotron radiation source. The Rietveld crystal structure refinement of the XRD data was carried out by the Jana 2006 program package.

The temperature-programmed reduction (H<sub>2</sub>-TPR) of  $R_{1.5}Ca_{0.5}NiO_4$  oxides was performed using a USGA device in an  $H_2:Ar = 1:20$  gas mixture at a flow rate of 30 cm<sup>3</sup> min<sup>-1</sup>. The temperature of the samples (~0.05 g) was increased to 950 °C at a heating rate of 5 °C min<sup>-1</sup>. The morphology of the powders was studied using a Carl Zeiss NVision 40 scanning electron microscope (Carl Zeiss SMT AG, Oberkochen, Germany).

### 2.3. Catalytic Experiments

The catalytic tests of the DRM and POM reactions were carried out in a quartz glass flow fixed-bed reactor (18 mm internal diameter, 300 mm length). The temperature inside the reactor was measured by a thermocouple placed in a special pocket running lengthwise along the reactor axis, 8 mm in diameter. A 0.2 g sample of catalyst (100–250 mesh fraction) was placed in the middle part of the reactor between two quartz glass rods. The free space in the reactor was filled with closely packed quartz glass fillers in order to eliminate gas-phase reactions outside the catalyst. The catalytic tests were carried out at atmospheric pressure in the absence of dilution with inert gas. The catalyst was first heated in hydrogen flow at 10 °C min<sup>-1</sup> to 900 °C. Then, the gas stream was switched to a mixture of  $CH_4/CO_2 = 1/1$  or  $CH_4/O_2 = 2/1$ . According to the results of our previous studies (Figure 3 in [36]), the GHSV values were set at 16 and 12 L g<sup>-1</sup> h<sup>-1</sup> for DRM and POM, respectively. No dilution of the feed flow by the inert gas was applied. The catalytic experiments were performed consecutively at 900, 800, 700, and 600 °C by maintaining the preselected temperatures for 1–5 h. After the analysis, the furnace was switched off, and the catalyst was cooled to room temperature over 3–4 h in pure N<sub>2</sub>.

The methane conversion ( $X$ ), product selectivity ( $S$ ), and yield ( $Y$ ) of the products are defined as follows:

$$X(CH_4, \%) = \frac{\text{moles of } CH_4 \text{ converted}}{\text{moles of } CH_4 \text{ in feed}} \times 100 \quad (1)$$

$$S(\text{CO} \cdot \text{or} \cdot \text{CO}_2, \%, \cdot \text{POM}) = \frac{\text{moles} \cdot \text{of} \cdot \text{CO} \cdot \text{in} \cdot \text{products}}{\text{moles} \cdot \text{of} \cdot \text{CH}_4 \cdot \text{converted}} \times 100 \quad (2)$$

$$S(\text{CO}, \%, \cdot \text{DRM}) = \frac{\text{moles} \cdot \text{of} \cdot \text{CO} \cdot \text{in} \cdot \text{products}}{\text{moles} \cdot \text{of} \cdot \text{CH}_4 + \text{CO}_2 \cdot \text{converted}} \times 100 \quad (3)$$

$$S(\text{H}_2, \%) = \frac{\text{moles} \cdot \text{of} \cdot \text{H}_2 \cdot \text{produced}}{2 \times \text{moles} \cdot \text{of} \cdot \text{CH}_4 \cdot \text{converted}} \times 100 \quad (4)$$

$$Y(\text{products}, \%) = \frac{X(\text{CH}_4, \%) \cdot S(\text{products}, \%)}{100} \quad (5)$$

$$C \text{ balance } (\%) = \frac{\text{moles} \cdot \text{of} \cdot \text{C} \cdot \text{in} \cdot \text{products}}{\text{moles} \cdot \text{of} \cdot \text{C} \cdot \text{in} \cdot \text{feed}} \times 100 \quad (6)$$

The number of moles of the feed gases and gaseous products of the reactions was calculated based on the measured volumetric velocity of the feeder gases and the products formed, as well as chromatography data, which makes it possible to fully take into account the stoichiometry of the reaction and the corresponding volume of expansion of the gaseous mixture of reagents.

### 3. Results and Discussion

#### 3.1. Synthesis of $R_{1.5}\text{Ca}_{0.5}\text{NiO}_4$

Single-phase  $\text{Nd}_{1.5}\text{Ca}_{0.5}\text{NiO}_4$ ,  $\text{Sm}_{1.5}\text{Ca}_{0.5}\text{NiO}_4$ , and  $\text{Eu}_{1.5}\text{Ca}_{0.5}\text{NiO}_4$  nickelates were obtained using a freeze-drying procedure similar to that in [15,16]. XRD study of the obtained complex oxides revealed that their crystal structure belonged to the orthorhombically distorted  $\text{K}_2\text{NiF}_4$  type. Detailed investigation of the obtained  $R_{1.5}\text{Ca}_{0.5}\text{NiO}_4$  crystal structure was performed using Rietveld refinement of the synchrotron powder diffraction data (Figure 1).

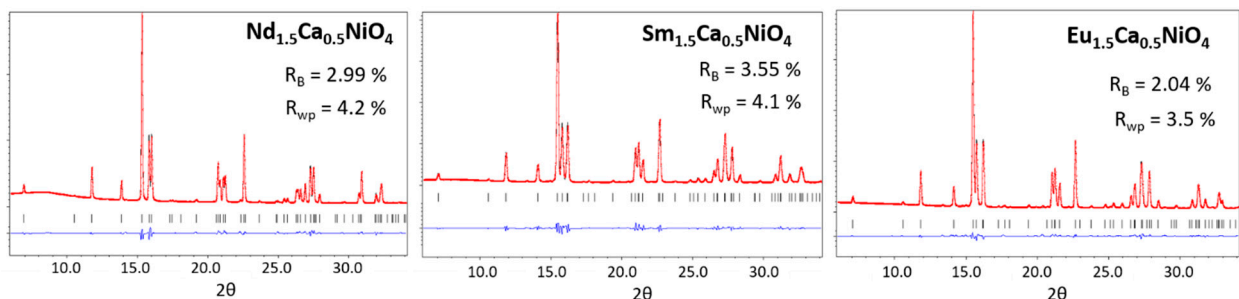


**Figure 1.** Rietveld refinement plots of the synchrotron data for  $\text{Nd}_{1.5}\text{Ca}_{0.5}\text{NiO}_4$ ,  $\text{Sm}_{1.5}\text{Ca}_{0.5}\text{NiO}_4$ , and  $\text{Eu}_{1.5}\text{Ca}_{0.5}\text{NiO}_4$ : observed (red), calculated (black) and difference (blue) curves. Bragg reflection positions are marked as short vertical lines below the observed and calculated data.

The orthorhombic  $\text{Cmce}$  model was assigned to each nickelate. This polymorph of the  $\text{K}_2\text{NiF}_4$  structure was previously observed for  $\text{Nd}_{2-x}\text{Ca}_x\text{NiO}_4$  solid solutions with Ca contents close to 0.5 [16]. In addition, the same structure type was found for  $\text{Sm}_{1.5}\text{Ca}_{0.5}\text{NiO}_4$  oxide in [37]. Information on the structure and properties of  $\text{Eu}_{1.5}\text{Ca}_{0.5}\text{NiO}_4$  was not found in the literature.

According to the Rietveld refinement data, the  $R_{1.5}\text{Ca}_{0.5}\text{NiO}_4$  unit cell  $c$  parameter decreased systematically from Nd to Eu (Figure 2a,b) in accordance with the decrease of the  $\text{R}^{3+}$  ionic radii [31,38]. The degree of orthorhombic distortion which can be estimated by the difference between the  $a$  and  $b$  parameters was found to increase in this series (Figure 2a). However, despite such considerable changes in unit cell dimensions, the observed Ni-O distances were almost the same within the  $R_{1.5}\text{Ca}_{0.5}\text{NiO}_4$  series (Figure 2c,d). This indicated that the valence states of Ni were highly likely to be the same for all discussed  $R_{1.5}\text{Ca}_{0.5}\text{NiO}_4$  compounds and similar to that for  $\text{Nd}_{1.5}\text{Ca}_{0.5}\text{NiO}_4$  wherein the mixed  $\text{Ni}^{2+}:\text{Ni}^{3+} = 1:1$  valence state of Ni was proposed [15]. Moreover, the fact that all of the  $R_{1.5}\text{Ca}_{0.5}\text{NiO}_4$

nickelates were characterized by the Cmce type of  $K_2NiF_4$  structure might be attributed to the nearly stoichiometric oxygen content in these complex oxides also observed for  $Nd_{1.5}Ca_{0.5}NiO_4$ , and thus correspond to the Ni formal oxidation state of 2.5 [39].

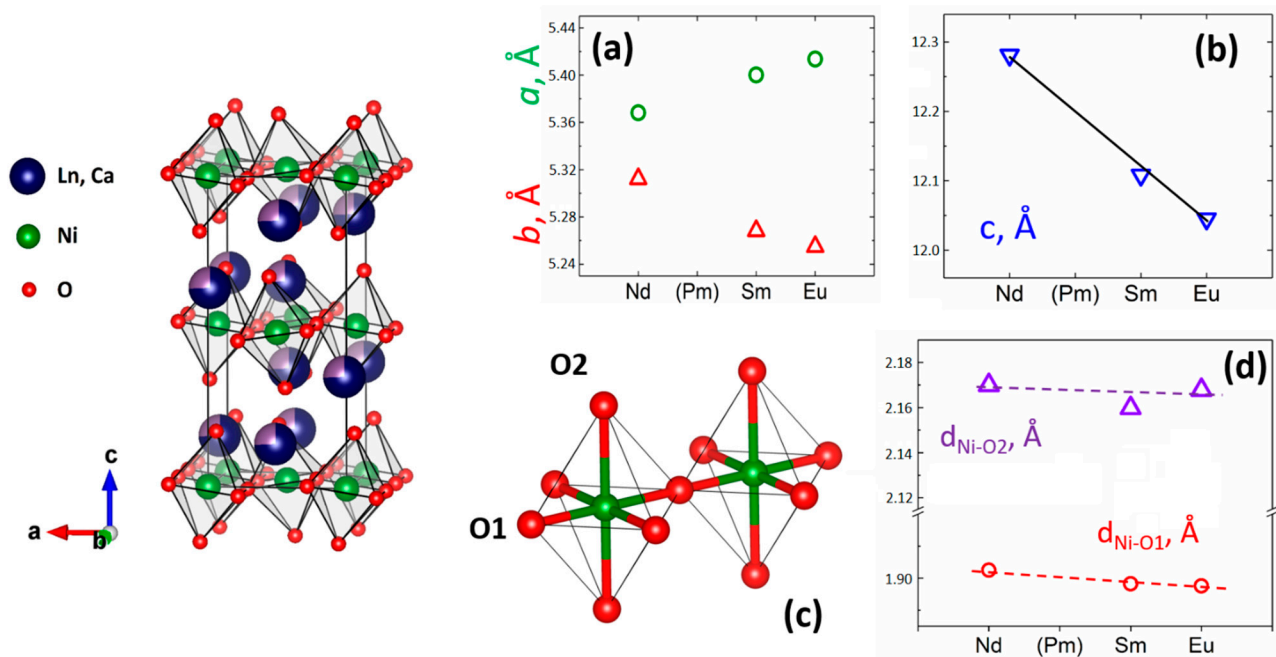


**Figure 2.** Representation of the Cmce lattice of the  $R_{1.5}Ca_{0.5}NiO_4$  crystal structure obtained by the Rietveld refinement (left); dependences of lattice parameters on the nickelate composition (a,b); representation of Ni octahedral coordination in the  $R_{1.5}Ca_{0.5}NiO_4$  structure obtained by the Rietveld refinement (c); dependences of Ni-O distances on the nickelate composition (d).

Therefore, the structure distortion in Nd-Sm-Eu nickelates is likely related to the corresponding rare earths' ionic radii effect, similar to that in  $ABO_3$  perovskites described by Goldschmidt's tolerance factor. Smaller  $R^{3+}$  cations corresponded to less-stable perovskite-like  $K_2NiF_4$  oxides. This decrease in the  $K_2NiF_4$ -like lattice stability correlates with a systematic increase in the temperature needed to obtain  $Nd_{1.5}Ca_{0.5}NiO_4$ ,  $Sm_{1.5}Ca_{0.5}NiO_4$ , and  $Eu_{1.5}Ca_{0.5}NiO_4$  nickelates (1000, 1100, and 1250 °C, respectively).  $Gd_{1.5}Ca_{0.5}NiO_4$  is less stable, so we could not obtain it even at 1350 °C (Supplementary Figures S1 and S2).

### 3.2. Synthesis of Ni/( $R_2O_3$ , CaO) Composites

According to the temperature-programmed reduction ( $H_2$ -TPR) data, the reduction of the  $Sm_{1.5}Ca_{0.5}NiO_4$  and  $Eu_{1.5}Ca_{0.5}NiO_4$  complex oxides occurred in a similar way to that of  $Nd_{1.5}Ca_{0.5}NiO_4$ ; the latter was described in [15]. All three  $H_2$ -TPR profiles consisted of two maxima of  $H_2$  consumption, one at 450–600 °C and one at 700–800 °C (Figure 3a). These maxima can be attributed to the partial and complete reduction of the complex oxide, respectively. According to previous research data [15,16], the complete reduction of  $K_2NiF_4$  nickelates led to the mixture of Ni metal and individual rare/alkaline earths' oxides; this was the case for  $Sm_{1.5}Ca_{0.5}NiO_4$  and  $Eu_{1.5}Ca_{0.5}NiO_4$ , too. Analysis of the XRD data showed that all of the nickelates under investigation were completely reduced at 900 °C in  $H_2$  flow. All of the reduced samples were composed of Ni metal (ICCD#: 00-004-0850), CaO (ICCD#: 00-037-1497), and different polymorphs of  $R_2O_3$  (Figure 3b). For the Nd-containing sample, it was h- $Nd_2O_3$  (ICCD#: 00-041-1089); for the Sm-containing sample, it was c- $Sm_2O_3$  (ICCD#: 00-015-0813); and for Eu-containing sample, it was a mixture of cubic (ICCD#: 00-034-0392) and monoclinic (ICCD#: 00-034-0072)  $Eu_2O_3$  modifications.

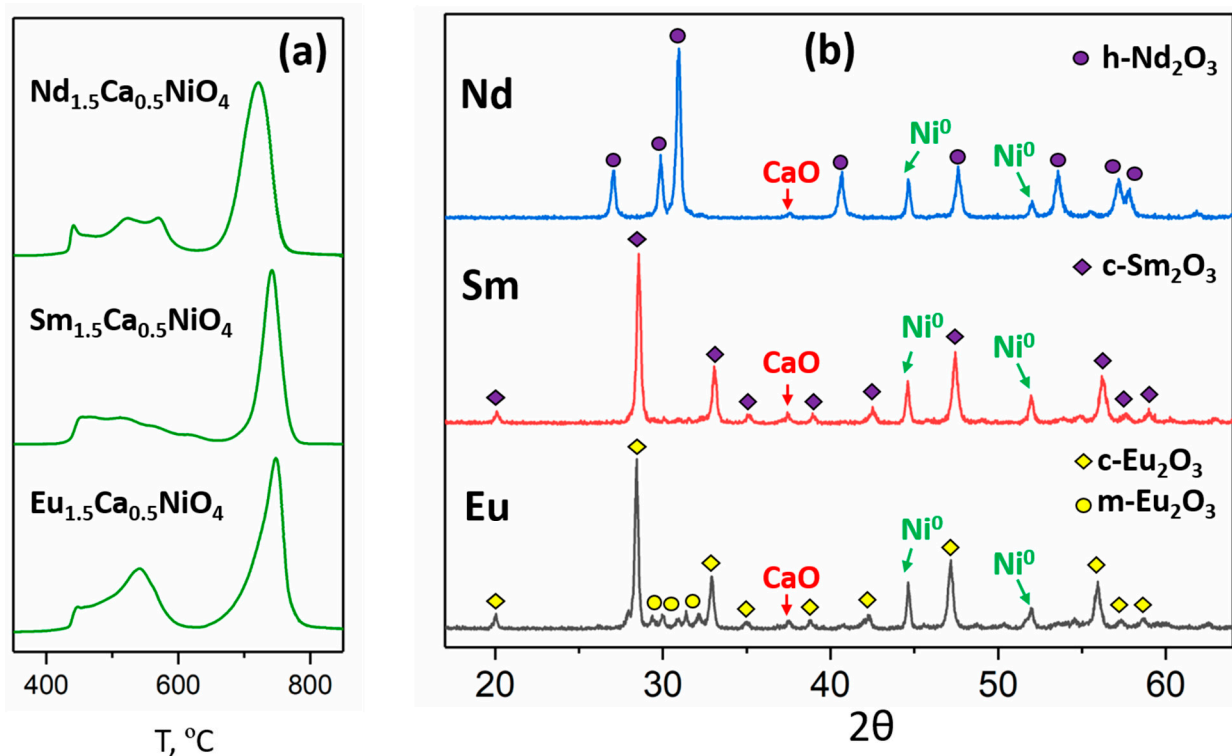


**Figure 3.** H<sub>2</sub>-TPR profiles for Nd<sub>1.5</sub>Ca<sub>0.5</sub>NiO<sub>4</sub>, Sm<sub>1.5</sub>Ca<sub>0.5</sub>NiO<sub>4</sub>, and Eu<sub>1.5</sub>Ca<sub>0.5</sub>NiO<sub>4</sub> (a); XRD plots of the nickelates' reduction products at 900 °C (b).

The microstructure of the obtained Ni/(R<sub>2</sub>O<sub>3</sub>,CaO) composites was investigated using the SEM technique. It has been established that the morphology transformations during the R<sub>1.5</sub>Ca<sub>0.5</sub>NiO<sub>4</sub> complete reduction were similar to those observed in the case of Nd<sub>2-x</sub>Ca<sub>x</sub>NiO<sub>4</sub> and Nd<sub>2-y</sub>Ca<sub>y</sub>Co<sub>1-x</sub>Ni<sub>x</sub>O<sub>4</sub> reduction [15,16,36].

According to the SEM micrographs, the initial R<sub>1.5</sub>Ca<sub>0.5</sub>NiO<sub>4</sub> samples consisted of 2–3 μm crystallites with clear traces of the intense sintering which was induced by the relatively high annealing temperatures that occurred during their synthesis (Figure 4, ×25k). The composites obtained by the reduction of R<sub>1.5</sub>Ca<sub>0.5</sub>NiO<sub>4</sub> were also characterized by a similar ceramic-like morphology. They were constructed by large, closely packed 2–3 μm grains of nearly polygonal shape separated by the distinct grain boundaries; the surface of such grains was uniformly covered by spherical nanoparticles.

This type of morphology is usually observed for redox exsolution products, wherein the grains of the partially reduced oxide precursors are decorated with uniformly distributed metal nanoparticles [11–14]. The same microstructural pattern has been observed for complete reduction products of Nd<sub>2-x</sub>Ca<sub>x</sub>NiO<sub>4</sub>, for which ~25 nm Ni particles were anchored to the surface of dense agglomerates of Nd<sub>2</sub>O<sub>3</sub> and CaO oxides [16]. These composites inherited the morphology of the initial nickelate powder. In the present study, Ni/(Nd<sub>2</sub>O<sub>3</sub>,CaO) composite also inherited the morphology of the sintered Nd<sub>1.5</sub>Ca<sub>0.5</sub>NiO<sub>4</sub> sample. According to our previous studies [15,16], these large “grains” corresponded to the dense aggregates of Nd<sub>2</sub>O<sub>3</sub> and CaO, while spherical particles anchored to their surface corresponded to the Ni metal phase. The same microstructure was observed for the Ni/(Sm<sub>2</sub>O<sub>3</sub>,CaO) and Ni/(Eu<sub>2</sub>O<sub>3</sub>,CaO) composites obtained by the reduction of Sm<sub>1.5</sub>Ca<sub>0.5</sub>NiO<sub>4</sub> and Eu<sub>1.5</sub>Ca<sub>0.5</sub>NiO<sub>4</sub>, respectively, which has never been described before.

Statistical analysis of the Ni particles size in SEM micrographs of the Ni/(R<sub>2</sub>O<sub>3</sub>,CaO) composites (Figure 4; ×100k, ×250k) demonstrated that all of the samples were characterized by similar Ni size distributions, with maxima around 24 nm and little or no rare earth effect. This shows the primary role of the similar R<sub>1.5</sub>Ca<sub>0.5</sub>NiO<sub>4</sub> reduction conditions detected by the TPR technique and the equal H<sub>2</sub> annealing temperatures that led to the similar morphology of the Ni/(R<sub>2</sub>O<sub>3</sub>,CaO) composites.

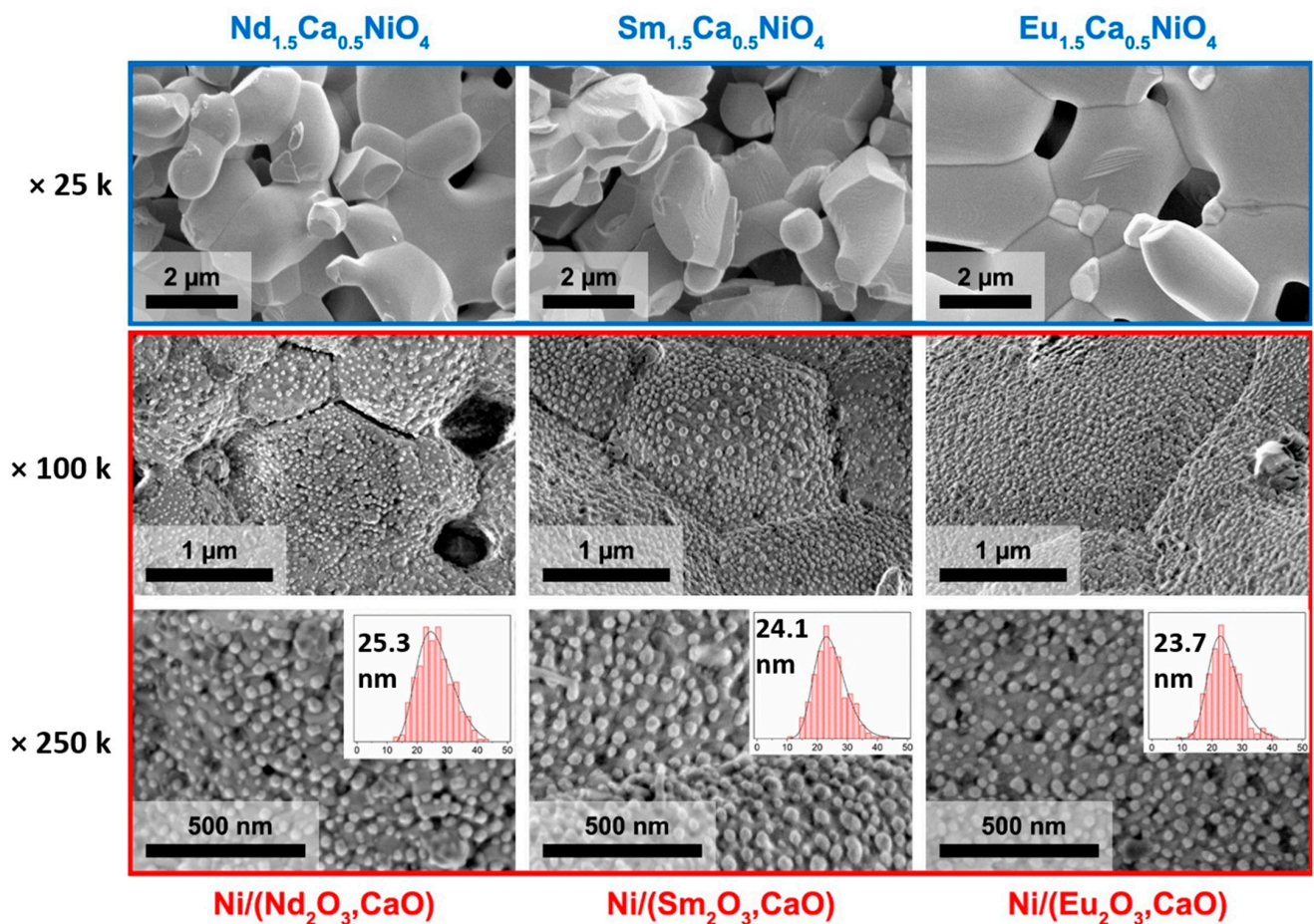


**Figure 4.** SEM micrographs of the initial  $R_{1.5}Ca_{0.5}NiO_4$  oxides ( $\times 25k$ ) and nanocomposites obtained by the reduction of the corresponding nickelates at  $900\text{ }^\circ\text{C}$  ( $\times 100k$ ;  $\times 250k$ ).

### 3.3. DRM and POM Catalytic Testing

The catalytic performance of the obtained  $Ni/(R_2O_3,CaO)$  nanocomposites in DRM and POM processes at  $600\text{--}900\text{ }^\circ\text{C}$  was evaluated using a flow reactor and undiluted  $CH_4/CO_2$  and  $CH_4/O_2$  mixtures, respectively. It was found during DRM testing that all of the presented samples demonstrated relatively high catalytic activity compared with other Ni-based catalysts (Figure 5a,b) [1,2]. However, the values of the CO and  $H_2$  yields decreased within the Nd-Sm-Eu series from  $\sim 90\%$  for the Nd-containing sample to  $\sim 70\%$  for the Eu-containing catalyst at  $800\text{ }^\circ\text{C}$ .

The opposite tendency was observed during POM testing of the  $Ni/(R_2O_3,CaO)$  nanocomposite catalysts (Figure 5c,d).  $Ni/(Sm_2O_3,CaO)$  and  $Ni/(Eu_2O_3,CaO)$  samples demonstrated slightly higher  $CH_4$  conversion than the Nd-containing catalyst. Notably, that  $Ni/(Nd_2O_3,CaO)$  nanocomposite showed better CO selectivity at  $700$  and  $800\text{ }^\circ\text{C}$  in the POM reaction.

The essential feature of such metal–oxide composites produced by the exsolution-like synthesis is the reproducibility of their catalytic performance in the course of redox processes taking place in the active phase. It was determined that this was the case for  $R_{1.5}Ca_{0.5}NiO_4$  reduction products. It was reported previously [16] that  $Ni/(Nd_2O_3,CaO)$  nanocomposites obtained via  $Nd_{2-x}Ca_xNiO_4$  decomposition remained chemically stable during DRM reaction at  $600\text{--}900\text{ }^\circ\text{C}$ , whereas the POM environment caused the oxidation of Ni particles to NiO oxide. Thus, the same tendency is likely presented in the case of  $Ni/(R_2O_3,CaO)$  catalysts. Cyclic DRM catalytic testing (Figure 6a) revealed that the high performance of  $Ni/(Eu_2O_3,CaO)$  nanocomposite was completely restored when the reaction temperature was raised back to  $900\text{ }^\circ\text{C}$ . Cyclic POM testing of  $Ni/(Sm_2O_3,CaO)$  catalyst

(Figure 6b) also demonstrated a similar restoration of the CO and H<sub>2</sub> yields to their high initial values after being reheated, despite the oxidation processes that took place at lower temperatures. It is notable that the decrease of R<sub>1.5</sub>Ca<sub>0.5</sub>NiO<sub>4</sub> stability discussed before in Section 3.1 should completely suppress the resynthesis process, which drastically decreased the catalytic activity of the similar Co-containing composites in the POM reaction [15].

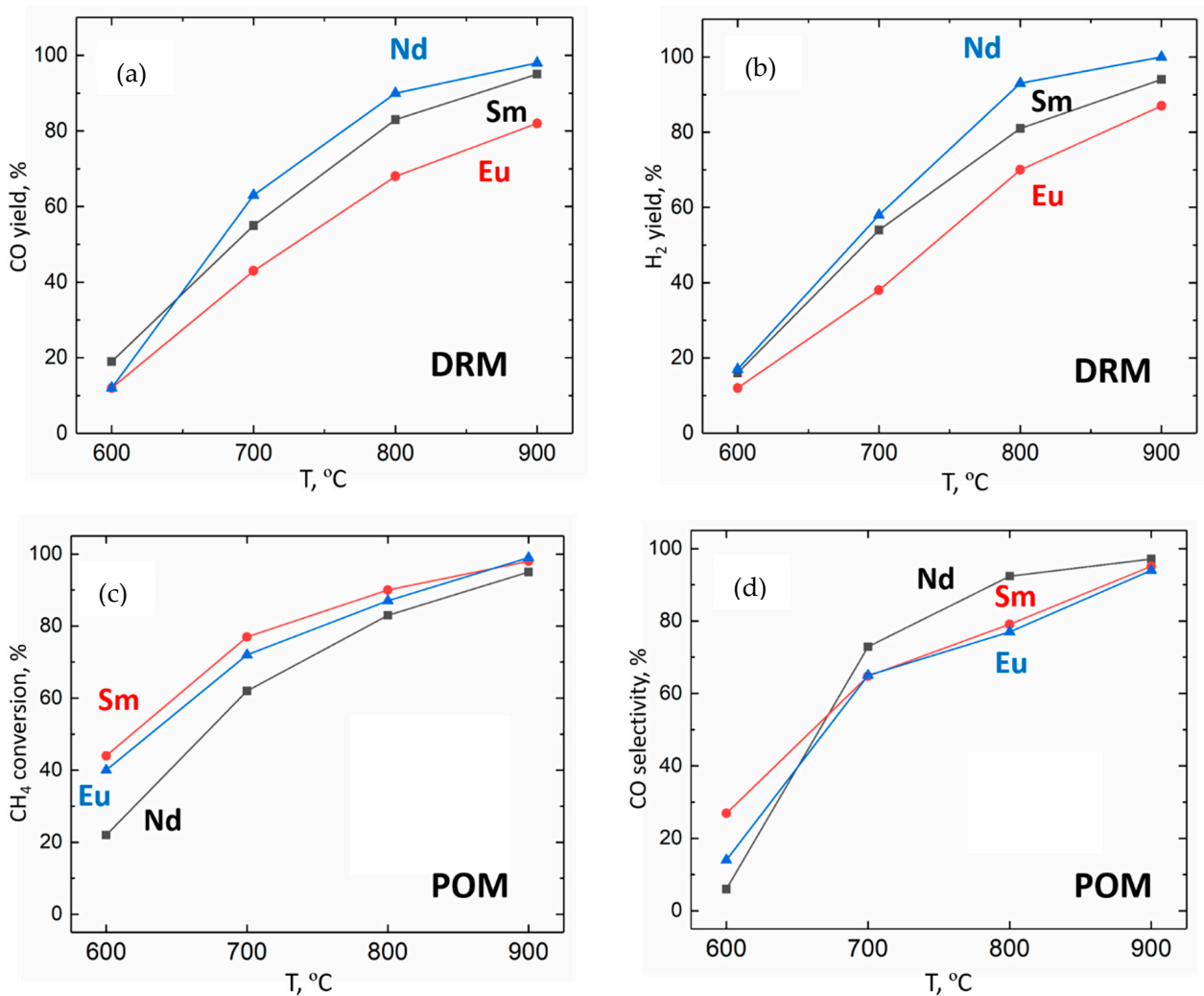


**Figure 5.** The dependences of CO and H<sub>2</sub> yields in the DRM reaction on the temperature for Ni/(R<sub>2</sub>O<sub>3</sub>, CaO) nanocomposites (a,b). Dependences of CH<sub>4</sub> conversion and CO selectivity in the POM reaction on the temperature for Ni/(R<sub>2</sub>O<sub>3</sub>, CaO) nanocomposites (c,d).

Since the microstructures of all of the obtained materials were found to be similar, the difference in the catalytic DRM and POM performance can likely be attributed to the difference in their Ni/(R<sub>2</sub>O<sub>3</sub>, CaO) compositions. The possible effects of various rare earth oxides on the catalytic activity in DRM and POM reactions were discussed in [23–25]. In most cases, the role of R<sub>2</sub>O<sub>3</sub> oxide in DRM reactions is usually associated with CO<sub>2</sub> capture and activation. Thus, a higher basicity of the rare earth oxide provides more efficient CO<sub>2</sub> chemisorption, leading to higher catalytic activity. As the basicity decreases in the Nd<sub>2</sub>O<sub>3</sub>–Sm<sub>2</sub>O<sub>3</sub>–Eu<sub>2</sub>O<sub>3</sub> series, it seems reasonable to suppose a parallel decrease in the CO<sub>2</sub> activation efficiency. This is likely the case for exsolved Ni/(R<sub>2</sub>O<sub>3</sub>, CaO) nanocomposites-containing samples—both CO and H<sub>2</sub> yields decrease from Nd to Eu.

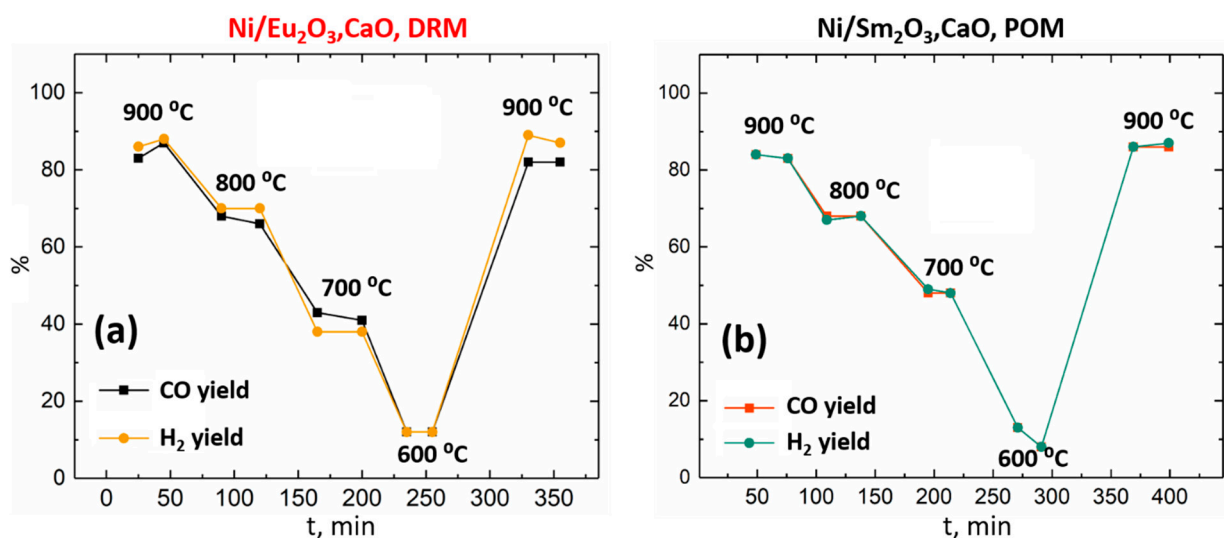


**Figure 6.** Temporal dependence of CO and H<sub>2</sub> yields in DRM (a) and POM (b) reactions at different temperatures for Ni/(Eu<sub>2</sub>O<sub>3</sub>,CaO) and Ni/(Sm<sub>2</sub>O<sub>3</sub>,CaO) catalysts, respectively.

In the case of POM reactions, the roles of the rare earth oxides are different at the different stages of this complex multistage process. These oxides are often considered as a source of active lattice oxygen, providing total oxidation of methane to CO<sub>2</sub>—the first step to the partial oxidation products. For instance, the role of La<sub>2</sub>O<sub>3</sub> in POM reactions over Ni/La<sub>2</sub>O<sub>3</sub> catalyst is discussed in detail in [28]; the involvement of Nd<sub>2</sub>O<sub>3</sub> lattice oxygen is also reported in [40]. Thus, the observed differences in the CH<sub>4</sub> conversion between Ni/(Nd<sub>2</sub>O<sub>3</sub>,CaO) and Sm- and Eu-containing catalysts can be attributed to the different efficiencies of total oxidation. Most likely, Sm<sub>2</sub>O<sub>3</sub> and Eu<sub>2</sub>O<sub>3</sub> provide a higher yield of the intermediate CH<sub>4</sub> → CO<sub>2</sub> transformation in comparison with Nd<sub>2</sub>O<sub>3</sub> oxide. This effect led to the slight but distinct increase in the methane conversion values at 700–800 °C. On the other hand, the increase in CO<sub>2</sub> yield in the first POM reaction step can cause an increase in the overall CO<sub>2</sub> yield, lowering the CO selectivity. This hypothesis was found to be in good agreement with the experimental data; CO selectivity values for Ni/(Nd<sub>2</sub>O<sub>3</sub>,CaO) at 800 °C are ~20 % higher than those for Ni/(Sm<sub>2</sub>O<sub>3</sub>,CaO) and Ni/(Eu<sub>2</sub>O<sub>3</sub>,CaO) nanocomposites.

#### 4. Conclusions

Nd<sub>1.5</sub>Ca<sub>0.5</sub>NiO<sub>4</sub>, Sm<sub>1.5</sub>Ca<sub>0.5</sub>NiO<sub>4</sub>, and Eu<sub>1.5</sub>Ca<sub>0.5</sub>NiO<sub>4</sub> nickelates with perovskite-like K<sub>2</sub>NiF<sub>4</sub> structure were synthesized by freeze-drying technique; Eu<sub>1.5</sub>Ca<sub>0.5</sub>NiO<sub>4</sub> was obtained and described for the first time. Rietveld refinement of the synchrotron diffraction data proved the formation of Cmce structure modification with a gradual increase of the orthorhombic distortion grade from Nd- to Eu-containing oxide.

All of the obtained nickelates demonstrated similar complete reduction conditions determined using the H<sub>2</sub>-TPR technique. The reduction processes of Sm<sub>1.5</sub>Ca<sub>0.5</sub>NiO<sub>4</sub> and Eu<sub>1.5</sub>Ca<sub>0.5</sub>NiO<sub>4</sub> and the properties of their reduction products are also described for the first time. The composites obtained by R<sub>1.5</sub>Ca<sub>0.5</sub>NiO<sub>4</sub> reduction at 900 °C consisted of Ni metal, CaO, and corresponding R<sub>2</sub>O<sub>3</sub> oxides. The microstructure of as-obtained metal-oxide nanocomposites is very similar to the typical microstructure of the redox exsolution products: the crystallites of the oxide phases formed dense agglomerates decorated by the uniformly distributed ~25 nm anchored particles of Ni metal. The identical microstructure of all of the Ni/(R<sub>2</sub>O<sub>3</sub>,CaO) nanocomposites in the study can be attributed to the similar temperatures of their reduction.

Catalytic testing of the obtained Ni/(R<sub>2</sub>O<sub>3</sub>,CaO) materials in DRM and POM reactions proved their excellent activity in both processes. Comparative analysis of their catalytic properties demonstrated a gradual decrease of the syngas yield in the DRM process within the Ni/(Nd<sub>2</sub>O<sub>3</sub>,CaO)–Ni/(Sm<sub>2</sub>O<sub>3</sub>,CaO)–Ni/(Eu<sub>2</sub>O<sub>3</sub>,CaO) series. This effect is most likely

related to the decrease of the corresponding rare earth oxides' basicity and less-efficient CO<sub>2</sub> activation. During POM testing, a slight increase in the methane conversion was detected for the same series. The probable nature of this effect could deal with the intensity increase of the total oxidation of methane, which led to the considerable decrease in the CO selectivity of Ni/(Sm<sub>2</sub>O<sub>3</sub>,CaO) and Ni/(Eu<sub>2</sub>O<sub>3</sub>,CaO) in comparison with the Ni/(Nd<sub>2</sub>O<sub>3</sub>,CaO) sample.

**Supplementary Materials:** The following supporting information can be downloaded at: <https://www.mdpi.com/article/10.3390/ma15207265/s1>.

**Author Contributions:** Conceptualization, O.A.S. and A.G.D.; methodology, O.A.S., S.A.M., A.S.L. and G.N.M.; validation, O.A.S., A.S.L. and G.N.M.; investigation, S.A.M., G.M.T., I.E.M. and I.V.R.; data curation, S.A.M., A.S.L. and R.D.S.; formal analysis, S.A.M., A.S.L. and R.D.S.; software, S.A.M. and R.D.S.; resources, O.A.S. and A.S.L.; writing—original draft, O.A.S. and S.A.M.; Writing—review and editing, O.A.S., G.N.M. and A.S.L.; visualization, S.A.M. and G.M.T.; project administration, O.A.S. and A.G.D.; funding acquisition, O.A.S.; supervision, A.G.D. All authors have read and agreed to the published version of the manuscript.

**Funding:** This study is supported by the Russian Foundation for Basic Research (grants 19-33-90141 and 20-03-00723). The Russian Science Foundation grant 20-13-00138 is gratefully acknowledged for the support of the DRM studies. The POM studies were carried out within the state funding of TIPS RAS. The Moscow State University program of development is gratefully acknowledged for the partial support of the instrumental studies. SEM images were obtained at the IGIC RAS Joint Research Centre for Physical Methods of Research.

**Conflicts of Interest:** The authors declare no conflict of interest.

## References

1. Li, M.; Sun, Z.; Hu, Y.H. Catalysts for CO<sub>2</sub> reforming of CH<sub>4</sub>: A review. *J. Mater. Chem. A* **2021**, *9*, 12495. [CrossRef]
2. Zhang, X.; Vajglova, Z.; Maki-Arvela, P.; Peurla, M.; Palonen, H.; Murzin, D.Y.; Tungatarova, S.A.; Baizhumanova, T.S.; Aubakirov, Y.A. Mono- and Bimetallic Ni-Co Catalysts in Dry Reforming of Methane. *ChemistrySelect* **2021**, *6*, 3424–3434. [CrossRef]
3. Arku, P.; Regmi, B.; Dutta, A. A review of catalytic partial oxidation of fossil fuels and biofuels: Recent advances in catalyst development and kinetic modeling. *Chem. Eng. Res. Design* **2018**, *136*, 385–402. [CrossRef]
4. Alshihri, S.; Almegren, H. Advances in Selective Oxidation of Methane; InTechOpen, London, UK, 2020. Available online: <https://www.intechopen.com/chapters/67664> (accessed on 14 October 2022).
5. Konnerth, H.; Matsagar, B.M.; Chen, S.S.; Pechtl, M.H.G.; Shieh, F.K.; Wu, K.C.W. Metal-organic framework (MOF)-derived catalysts for fine chemical production. *Coord. Chem. Rev.* **2020**, *416*, 213319. [CrossRef]
6. Liao, Y.T.; Chi, N.V.; Ishiguro, N.; Young, A.P.; Tsung, C.K.; Wu, K.C.-W. Engineering a homogeneous alloy-oxide interface derived from metal-organic frameworks for selective oxidation of 5-hydroxymethylfurfural to 2,5-furandicarboxylic acid. *Appl. Catal. B* **2020**, *270*, 118805. [CrossRef]
7. Elbadawi, A.H.; Ge, L.; Li, Z.; Liu, S.; Wang, S.; Zhu, Z. Catalytic partial oxidation of methane to syngas: Review of perovskite catalysts and membrane reactors. *Catal. Rev.* **2021**, *63*, 1–67. [CrossRef]
8. Wang, C.; Wang, Y.; Chen, M.; Liang, D.; Yang, Z.; Cheng, W.; Tang, Z.; Jun Wang, J.; Zhang, H. Recent advances during CH<sub>4</sub> dry reforming for syngas production: A mini review. *Int. J. Hydrogen Energy* **2021**, *46*, 5852–5874. [CrossRef]
9. Nishihata, Y.; Mizuki, J.; Akao, T.; Tanaka, H.; Uenishi, M.; Kimura, M.; Okamoto, T.; Hamada, N. Self-regeneration of a Pd-perovskite Catalyst for Automotive Emissions Control. *Nature* **2002**, *418*, 164–167. [CrossRef] [PubMed]
10. Tsekouras, G.; Miller, D.N.; MeGnard, H.; Irvine, J.T.S. In situ growth of nanoparticles through control of non-stoichiometry. *Nat. Chem.* **2013**, *5*, 916–923.
11. Neagu, D.; Oh, T.S.; Miller, D.N.; MeGnard, H.; Bukhari, S.M.; Gamble, S.R.; Gorte, R.J.; Vohs, J.M.; Irvine, J.T.S. Nano-socketed nickel particles with enhanced coking resistance grown in situ by redox exsolution. *Nat. Comm.* **2015**, *6*, 8120. [CrossRef]
12. Kwon, O.; Joo, S.; Choi, S.; Sengodan, S.; Kim, G. Review on exsolution and its driving forces in perovskites. *J. Phys. Energy* **2020**, *2*, 032001. [CrossRef]
13. Kousi, K.; Neagu, D.; Bekris, L.; Papaioannou, E.I.; Metcalfe, I.S. Endogenous Nanoparticles Strain Perovskite Host Lattice Providing Oxygen Capacity and Driving Oxygen Exchange and CH<sub>4</sub> Conversion to Syngas. *Angew. Chem. Int. Ed.* **2020**, *59*, 2510–2519. [CrossRef] [PubMed]
14. Shah, S.; Sayono, S.; Junzunza, J.; Pan, R.; Xu, M.; Pan, X.; Gilliard-AbdulAziz, K.L. The effects of stoichiometry on the properties of exsolved Ni-Fe alloy nanoparticles for dry methane reforming. *AIChE J.* **2020**, *66*, e17078. [CrossRef]

15. Shlyakhtin, O.A.; Malyshev, S.A.; Loktev, A.S.; Mazo, G.N.; Garshev, A.V.; Chumakov, R.G.; Dedov, A.G. Synthesis and decomposition of  $\text{Nd}_{2-y}\text{Ca}_y\text{Co}_{1-x}\text{Ni}_x\text{O}_4$ : The effect of resynthesis on the catalytic performance of decomposition products in the partial oxidation of methane. *ACS Appl. Energy Mater.* **2021**, *4*, 7661–7673. [[CrossRef](#)]
16. Malyshev, S.A.; Shlyakhtin, O.A.; Loktev, A.S.; Mazo, G.N.; Timofeev, G.M.; Mukhin, I.E.; Kaplin, I.Y.; Svetogorov, R.D.; Valeev, R.G.; Dedov, A.G. Exsolution-like synthesis of Ni/( $\text{Nd}_2\text{O}_3$ , CaO) nanocomposites from  $\text{Nd}_{2-x}\text{Ca}_x\text{NiO}_4$  precursors for catalytic applications. *J. Solid State Chem.* **2022**, *312*, 123267. [[CrossRef](#)]
17. Bhattar, S.; Ashrafal Abedin, M.; Kanitkar, S.; Spivey, J.J. A review on dry reforming of methane over perovskite derived catalysts. *Catal Today* **2021**, *365*, 2–23. [[CrossRef](#)]
18. Cihlar, J., Jr.; Vrba, R.; Castkova, K.; Cihlar, J. Effect of transition metal on stability and activity of La-Ca-M-(Al)-O (M = Co, Cr, Fe and Mn) perovskite oxides during partial oxidation of methane. *Int. J. Hydrogen Energy* **2017**, *42*, 19920–19934. [[CrossRef](#)]
19. Valderrama, G.; Kiennemann, A.; Urbina de Navarro, C.; Goldwasser, M.R.  $\text{LaNi}_{1-x}\text{Mn}_x\text{O}_3$  perovskite-type oxides as catalysts precursors for dry reforming of methane. *Appl. Catal. A* **2018**, *565*, 26–33. [[CrossRef](#)]
20. Shah, M.; Das, S.; Nayak, A.K.; Mondal, P.; Bordoloi, A. Smart designing of metal-support interface for imperishable dry reforming catalyst. *Appl. Catal. A* **2018**, *556*, 137.e54. [[CrossRef](#)]
21. Tathod, A.P.; Hayek, N.; Shpasser, D.; David, S.A.; Simakov, D.S.A.; Gazit, O.M. Mediating interaction strength between nickel and zirconia using a mixed oxide nanosheets interlayer for methane dry reforming. *Appl. Catal. B* **2019**, *249*, 106–115. [[CrossRef](#)]
22. Enger, B.C.; Lodeng, R.; Holmen, A. A review of catalytic partial oxidation of methane to synthesis gas with emphasis on reaction mechanisms over transition metal catalysts. *Appl. Catal. A* **2008**, *346*, 1–27. [[CrossRef](#)]
23. Al-Sayari, S.A. Recent Developments in the Partial Oxidation of Methane to Syngas. *Open Catalysis J.* **2013**, *6*, 17–28. [[CrossRef](#)]
24. Salaev, M.A.; Liotta, L.F.; Vodyankina, O.V. Lanthanoid-containing Ni-based catalysts for dry reforming of methane: A review. *Int. J. Hydrogen Energy* **2022**, *47*, 4489–4535. [[CrossRef](#)]
25. Ozazuwa, O.U.; Abidin, S.Z. An overview on the role of lanthanide series (rare earth metals) in  $\text{H}_2$  and syngas production from  $\text{CH}_4$  reforming processes. *Chem. Eng. Sci.* **2020**, *227*, 115863. [[CrossRef](#)]
26. Abdurashed, A.; Abdul Jalil, A.; Gambo, Y.; Ibrahim, M.; Umar Hambali, H.; Shahul Hamid, M.Y. A review on catalyst development for dry reforming of methane to syngas: Recent advances. *Renew. Sust. Energy Revs.* **2019**, *108*, 175–193. [[CrossRef](#)]
27. Song, X.; Dong, X.; Yin, S.; Wang, M.; Li, M.; Wang, H. Effects of Fe partial substitution of  $\text{La}_2\text{NiO}_4/\text{LaNiO}_3$  catalyst precursors prepared by wet impregnation method for the dry reforming of methane. *Appl. Catal. A* **2016**, *526*, 132–138. [[CrossRef](#)]
28. Bekheet, M.F.; Nezhad, P.D.K.; Bonmassar, N.; Schlicker, L.; Gili, A.; Praetz, S.; Gurlo, A.; Doran, A.; Gao, Y.; Heggen, M.; et al. Steering the Methane Dry Reforming Reactivity of Ni/ $\text{La}_2\text{O}_3$  Catalysts by Controlled In Situ Decomposition of Doped  $\text{La}_2\text{NiO}_4$  Precursor Structures. *ACS Catal.* **2021**, *11*, 43–59. [[CrossRef](#)] [[PubMed](#)]
29. Dama, S.; Ghodke, S.; Bobade, R.; Gurav, H.; Chilukuri, S. Tuning the dimensionality of layered  $\text{Sr}_{n+1}\text{Ti}_{n-x}\text{Ni}_x\text{O}_{3n+1}$  perovskite structures for improved activity in syngas generation. *J. Catalysis* **2018**, *360*, 27–39. [[CrossRef](#)]
30. Takeda, Y.; Nishijima, M.; Imanishi, N.; Kanno, R.; Yamamoto, O. Crystal chemistry and transport properties of  $\text{Nd}_{2-x}\text{A}_x\text{NiO}_4$  (A = Ca, Sr, or Ba,  $0 \leq x \leq 1.4$ ). *J. Solid State Chem.* **1992**, *96*, 72–83. [[CrossRef](#)]
31. Song, J.; Ning, D.; Boukamp, B.; Bassat, J.-M.; Bouwmeester, H.J.M. Structure, electrical conductivity and oxygen transport properties of Ruddlesden–Popper phases  $\text{Ln}_{n+1}\text{Ni}_n\text{O}_{3n+1}$  (Ln = La, Pr and Nd; n = 1, 2 and 3). *J. Mater. Chem. A* **2020**, *8*, 22206. [[CrossRef](#)]
32. Kim, D.; Lee, K.T. Effect of lanthanide (Ln = La, Nd, and Pr) doping on electrochemical performance of  $\text{Ln}_2\text{NiO}_{4+\delta}$  - YSZ composite cathodes for solid oxide fuel cells. *Ceram. Intern.* **2021**, *47*, 2493–2498. [[CrossRef](#)]
33. Pikalov, S.M.; Vedmid', L.B.; Filonova, E.A.; Pikalova, E.Y.; Lyagaeva, J.G.; Danilov, N.A.; Murashkina, A.A. High-temperature behavior of calcium substituted layered neodymium nickelates. *J. Alloys Compd.* **2019**, *801*, 558–567. [[CrossRef](#)]
34. Tarutin, A.P.; Gorshkov, M.Y.; Bainov, I.N.; Vdovin, G.K.; Vylkov, A.I.; Lyagaeva, J.G.; Medvedev, D.A. Barium-doped nickelates  $\text{Nd}_{2-x}\text{Ba}_x\text{NiO}_{4+\delta}$  as promising electrode materials for protonic ceramic electrochemical cells. *Ceram. Intern.* **2020**, *46*, 24355–24364. [[CrossRef](#)]
35. Gao, Z.; Ding, X.; Ding, D.; Ding, L. Infiltrated  $\text{Pr}_2\text{NiO}_4$  as promising bi-electrode for symmetrical solid oxide fuel cells. *Int. J. Hydrogen Energy* **2018**, *43*, 8953–8961. [[CrossRef](#)]
36. Dedov, A.G.; Loktev, A.S.; Komissarenko, D.A.; Mazo, G.N.; Shlyakhtin, O.A.; Parkhomenko, K.V.; Kiennemann, A.A.; Roger, A.-C.; Ishmurzin, A.V.; Moiseev, I.I. Partial oxidation of methane to produce syngas over a neodymium–calcium cobaltate-based catalyst. *Appl. Catal. A* **2015**, *489*, 140–146. [[CrossRef](#)]
37. Galayda, A.P.; Volkova, N.E.; Gavrilova, L.Y.; Balymov, K.G.; Cherepanov, V.A. Phase equilibria, structure and properties of intermediate phases in the  $\text{Sm}_2\text{O}_3$ – $\text{Fe}_2\text{O}_3$ –CoO and  $\text{Sm}_2\text{O}_3$ –CaO–CoO systems. *J. Alloys Compd.* **2017**, *718*, 288–297. [[CrossRef](#)]
38. Shannon, R.D. Revised effective ionic radii and systematic studies of interatomic distances in halides and chalcogenides. *Acta Cryst. A* **1976**, *32*, 751–767. [[CrossRef](#)]
39. Ceretti, M.; Wahyudi, O.; Andre, G.; Meven, M.; Villesuzanne, A.; Paulus, W. (Pr,Nd) $_2\text{NiO}_{4+\delta}$ : Reaction intermediates and redox behavior explored by in situ neutron powder diffraction during electrochemical oxygen intercalation. *Inorg. Chem.* **2018**, *57*, 4657–4666. [[CrossRef](#)]
40. Fang, X.; Zhang, J.; Liu, J.; Wang, C.; Huang, Q.; Xu, X.; Peng, H.; Liu, W.; Wang, X.; Zhou, W. Methane dry reforming over Ni/Mg-Al-O: On the significant promotional effects of rare earth Ce and Nd metal oxides. *J. CO<sub>2</sub> Util.* **2018**, *25*, 242–253. [[CrossRef](#)]